

Electrohydrodynamic printing of organic polymeric resistors on flat and uneven surfaces

Cite as: J. Appl. Phys. **120**, 084903 (2016); <https://doi.org/10.1063/1.4961421>

Submitted: 21 April 2016 . Accepted: 08 August 2016 . Published Online: 23 August 2016

Sepehr Maktabi, and Paul R. Chiarot



View Online



Export Citation



CrossMark

ARTICLES YOU MAY BE INTERESTED IN

[Drop-on-demand printing of conductive ink by electrostatic field induced inkjet head](#)

Applied Physics Letters **93**, 193508 (2008); <https://doi.org/10.1063/1.3020719>

[A field shaping printhead for high-resolution electrohydrodynamic jet printing onto non-conductive and uneven surfaces](#)

Applied Physics Letters **104**, 143510 (2014); <https://doi.org/10.1063/1.4871103>

[Mechanism of electrohydrodynamic printing based on ac voltage without a nozzle electrode](#)

Applied Physics Letters **94**, 173509 (2009); <https://doi.org/10.1063/1.3126957>

Journal of
Applied Physics

Special Topic:
Molecular Spintronics



Electrohydrodynamic printing of organic polymeric resistors on flat and uneven surfaces

Sepehr Maktabi and Paul R. Chiarot^{a)}

Department of Mechanical Engineering, State University of New York at Binghamton, Binghamton, New York 13902, USA

(Received 21 April 2016; accepted 8 August 2016; published online 23 August 2016)

In materials printing applications, the ability to generate fine droplets is critical for achieving high-resolution features. Other desirable characteristics are high print speeds, large stand-off distances, and minimal instrumentation requirements. In this work, a tunable electrohydrodynamic (EHD) printing technique capable of generating micron-sized droplets is reported. This method was used to print organic resistors on flat and uneven substrates. These ubiquitous electronic components were built using the commercial polymer-based conductive ink poly(3,4-ethylenedioxythiophene)-poly(styrenesulfonate) (PEDOT:PSS), which has been widely used in the manufacturing of organic electronic devices. Resistors with widths from 50 to 500 μm and resistances from 1 to 70 $\Omega/\mu\text{m}$ were created. An array of emission modes for EHD printing was identified. Among these, the most promising is the microdripping mode, where droplets 10 times smaller than the nozzle's inner diameter were created at frequencies in excess of 5 kHz. It was found that the ink flow rate, applied voltage, and stand-off distance all significantly influence the droplet generation frequency. In particular, the experimental results reveal that the frequency increases nonlinearly with the applied voltage. The non-Newtonian shear thinning behavior of PEDOT:PSS strongly influenced the droplet frequency. Finally, the topology of a 3-dimensional target substrate had a significant effect on the structure and function of a printed resistor. *Published by AIP Publishing.*

[<http://dx.doi.org/10.1063/1.4961421>]

I. INTRODUCTION

Organic printed electronics is an emerging technology that enables manufacturing of integrated circuits for applications such as displays, sensors, organic thin-film transistors, and photovoltaic cells.^{1–5} There has been significant research on the relationship between the properties of functional polymer materials and their chemical nature and supermolecular structure.^{6–10} Conductive polymers consisting of polythiophene are reported as one of the best choices for manufacturing flexible and organic electronic devices.^{11–17} These polymers are predominantly used in the fabrication of electrical patterns on substrates that cannot undergo rigorous thermal sintering, which is required for most metallic nanoparticle based inks. Many researchers have reported on the use of printing to fabricate stretchable tactile sensors.^{18,19} These are of particular interest for biomedical and robotic systems that require flexible and adaptable sensors that conform to the curvature of the host's structure. Polymeric composites are the most promising materials for the fabrication of these devices, because they show a huge variation in electrical resistance when subjected to mechanical deformation.

Poly(3,4-ethylenedioxythiophene)-poly(styrenesulfonate) (PEDOT:PSS) is commonly used in organic devices and has the potential to be a substitute for metallic materials due to its conductivity and high ductility.²⁰ PEDOT:PSS is regarded as a promising material for optoelectronic organic devices, because it enables cost-effective and transparent devices as

well as roll-to-roll mass production. It has been reported that a PEDOT:PSS film could serve as a transparent electrode for low-cost indium tin oxide (ITO)-free organic solar cells.²¹ The conductivity of the ink can be tuned by adding high boiling point solvents and polar compounds such as dimethyl sulfoxide (DMSO), ethylene glycol (EG), and sorbitol.^{22–25}

There are numerous techniques available to deposit thin layers of functional materials like PEDOT:PSS; e.g., dip and spin coating, spraying, chemical and physical vapor deposition, nanolithography, and inkjet printing. Spin-coating is widely used due to its high precision and reproducibility.²⁶ However, the spin-coating process cannot be used with large-area, flexible substrates or in high throughput roll-to-roll processing. Moreover, it is wasteful since it is a subtractive process, and the deposited material must be removed to create a desired pattern. An additive printing process such as inkjet printing allows material to be deposited only where it is required, enabling fabrication of customizable circuits.¹⁸

Inkjet printing has received a great deal of attention as an additive manufacturing technique because of its capability to deposit small volumes of liquid with high positional accuracy, high printing speed, no vacuum processing, and low cost.^{27–29} Liu *et al.* printed an insulating layer of polyimide combined with PEDOT:PSS to create electrodes for a parallel plate capacitor.³⁰ Chen *et al.* fabricated an all-polymer RC filter circuit using inkjet printing by depositing layers of PEDOT:PSS.³¹ They compared simulations of the printed circuit with the experimental results and reported that inkjet printing can offer lower costs over photolithography for micro-electronic devices. Kawase *et al.* reported an environmentally

^{a)}Author to whom correspondence should be addressed. Electronic mail: pchiarot@binghamton.edu

friendly inkjet printing methodology using a water-based PEDOT:PSS solution. They manufactured all-polymer circuits which contained not only organic thin film transistors (TFTs), but also interconnections, via holes, and resistors.³²

Many studies have been done on inkjet printing to optimize its parameters; e.g., nozzle temperature and diameter, vibration frequency of emission, jetting time periods, and voltages. However, the optimization of inkjet-printed PEDOT:PSS thin films has not been fully pursued. This is likely due to the inherent limitations of inkjet printing. For instance, ink formulation must be carefully controlled to enable high quality and high performance films to be produced by the inkjet process.^{33–35} Instrumentation requirements are demanding for inkjet printing, since actuation signals must be precisely timed to permit repeatable droplet generation.^{36,37} Since the stand-off distance between the nozzle and the substrate must be short (typically 2–3 mm),²⁸ it is difficult to use inkjet to print over uneven surfaces. The printed line width strongly depends on the droplet diameter, which is determined by the size of the nozzle inner diameter. Decreased line width and improved print resolution can be achieved by decreasing the nozzle size. However, smaller nozzles tend to clog easily due to fast evaporation rates at the nozzle tip, especially for nanoparticle-based inks.³⁸

Here, we report on a complementary printing technique based on electrohydrodynamic (EHD) microdroplet generation (Figure 1). In this process, liquid ink is steadily supplied to a section of capillary tubing pulled to a fine tip; i.e., the nozzle. A high potential is applied upstream of the nozzle opening relative to a ground plate. The target substrate is placed on top of this plate. The applied electric field penetrates into the liquid and induces an electric force on the mobile ions in the ink.

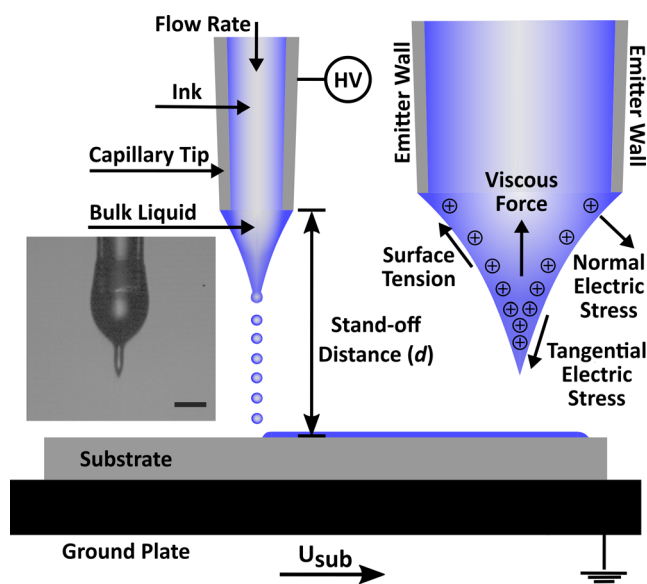


FIG. 1. Electrohydrodynamic (EHD) microdripping printing system. Mobile ions in the ink collect at the air-fluid interface and drive the emission of regular, uniform, and periodic droplets. The inset image is a micrograph showing the early stages of droplet formation (scale bar denotes 50 μm). The stand-off distance between the capillary tip and the substrate is constant. Ink is provided to the emitter using a syringe pump. The emitter is connected to a high voltage DC power supply. The substrate is placed on top of a ground plate moving at velocity U_{sub} .

The ions migrate towards the nozzle opening and accumulate at the surface of the pendant meniscus. This ultimately deforms the liquid meniscus into a conical shape. The mutual coulombic repulsion between these ions induces a tangential electric stress on the liquid surface. At a sufficiently high electric field, the electrostatic (Maxwell) stress overcomes the surface tension at the apex of the liquid meniscus and mass (i.e., droplets) is ejected at different emission regimes. A portion of the surface charge is also expelled as per the Rayleigh limit.

EHD printing offers low costs, simple processing, high-throughput, direct patterning, minimal instrumentation, and is well-suited for roll-to-roll processing. An EHD print head can produce droplets of uniform size that are significantly smaller than the size of the nozzle opening. The droplet size and dripping frequency can be easily modulated by the electric field applied to the liquid meniscus at the nozzle tip. The EHD printing technique does not require the use of a carrier gas as in ultrasonic spraying. The charged droplets are accelerated by the applied electric field as they approach the target surface, resulting in higher deposition accuracy.²⁶ In addition, EHD printing offers the ability to print over *uneven* topologies since it can be used at large stand-off distances. This technique has been shown to be compatible with organic electronic device fabrication.³⁹

To effectively use EHD printing to manufacture thin-film electronic components, the dynamics of the electrified fluid meniscus must be understood. The emissions mechanisms (i.e., emission regimes) depend upon the experimental parameters of an EHD printing system, yielding different modes of droplet generation; e.g., dripping, stable and pulsed single cone-jet, multicone-jet, microdripping, ramified jet, and spindle.^{40–46} In practice, small differences in experimental details, such as the shape or wettability of the capillary opening, may lead to the initiation of one mode over another and considerably change the characteristics of the emitted aerosols. The large set of interacting parameters (e.g., fluid properties, fluid flow rate, applied electric field, and ambient atmospheric conditions) makes it challenging to know beforehand the expected emission regime for a given set of operating conditions. For instance, for liquids with relatively high conductivities or at sufficiently high applied electric fields, the cone-jet formation zone is limited to the apex of the meniscus.⁴⁷ It was reported by Cloupeau and Prunet-Foch that for lower conductivities, the acceleration zone extends further toward the base of the cone.⁴⁰ In this case, the expression *convergent jet* used by Mutoh *et al.* would be more appropriate.⁴⁸ For applied electric fields slightly lower than that for which a single permanent jet is obtained, Juraschek and Röhlgen observed that the jet may only be emitted intermittently at “low” and “high” frequencies, creating the so-called pulsed single cone-jet mode.⁴⁹

The microdripping mode of EHD printing has several attractive features for use in materials printing. In particular, droplets are produced *continuously* with high periodicity and with highly uniform sizes ranging from 1 to 100 μm in diameter. Juraschek and Röhlgen observed this mode by applying an increasing electric potential to a drawn glass capillary tube.⁴⁹ They reported significantly different pulsations from those observed in the pulsed single cone-jet regime, which

increased with the field potential. This behavior was described as the periodic detachments of droplets from the apex of the bulk fluid at the capillary tip, which interrupts the discharge. Cloupeau and Prunet-Foch called this mass emission mode *microdripping* because the emission takes place drop-by-drop as in the conventional dripping mode; however, the droplets have a much smaller diameter than the capillary orifice.⁴⁰

Microdripping mode and cone-jet mode can appear under identical experimental conditions. It is reported that the frequency of oscillation in microdripping mode (which is in the kHz range) increases in a nonlinear fashion with the electric field.^{40,50,51} At higher potentials, there is a transition zone in which one spraying mode may replace the other, each being maintained for a rather long period. However, the range of conditions under which microdripping appears is much smaller than that of cone-jet mode. The establishment of microdripping mode is observed only for low flow rates and relatively low liquid ink conductivity.

The goal of this study was to improve our understanding of the processing-structure-property relationship of EHD printing of polymer-based inks. We explored the use of microdripping mode to create monodispersed droplets using the conductive ink PEDOT:PSS. We provide a theoretical explanation of microdripping mode and establish the relationship between the operating parameters (e.g., applied voltage, stand-off distance, and ink flow rate) and the EHD regimes. The influence of the operating parameters on droplet generation frequency is determined. Finally, the geometric characteristics and functionality of resistors created using EHD printing on flat and uneven substrates are investigated. This comprehensive study covers the entirety of the EHD printing technique, from processing through to the structure and properties of a printed line.

II. EXPERIMENTS

A unique feature of EHD printing is its modest instrumentation requirements (Figure 1). High temperatures and pressure, complex function generators, and vacuum are not required for printing. The field-enhanced microdripping mode originates from the edge of a glass capillary tube emitter with an inner diameter of $65 \pm 5 \mu\text{m}$. As shown in Figure 1, the glass capillary tube is oriented vertically and emits downward. This arrangement is preferable to a horizontal orientation to prevent excessive wetting of the tube at low voltages. It also simplifies the printing fixture since the stage platform can be oriented horizontally. The wettability of the entire capillary tip can be tuned by sputter-deposition of a thin layer of gold⁹ or by silanization. However, in this study, the glass capillary tube was left untreated since this was found to provide a stable meniscus and uniform, repeatable droplets.

The glass capillary tube was held in a manifold and fixed to a linear stage to control the stand-off distance between the nozzle and the substrate. The stand-off distance was maintained at 3, 5, and 10 mm. Ink was provided to the emitter using a 1 ml syringe loaded into a syringe pump (Chemxyx) through teflon tubing. The ink supply to the orifice

was fixed at three flow rates: 0.2, 0.8, and $1.2 \mu\text{l/min}$. The emitter was connected to a high voltage DC power supply (Spellman) via a port in the manifold at the upstream end of the glass tubing. Voltages between 2 kV and 4 kV at positive polarity were used to form the field enhanced micron-sized droplets. It is reported that the droplet emission is less disturbed by corona discharges with a positive polarity at the capillary tip.^{40,52} A 10 kV relay (Gigavac) was used to rapidly activate/deactivate the high voltage. The substrate was placed on top of a ground plate affixed to a two-axis linear stage (Aerotech). The stage was used to position (horizontally) the substrate relative to the stationary emitter at velocities in the range of 2–50 mm/s. The entire system (high voltage, linear stages, and machine vision systems) was controlled using LABVIEW.

Poly(3,4-ethylenedioxythiophene)-poly(styrenesulfonate) (PEDOT:PSS) commercial ink at 0.8 vol. % in water was used as received (Sigma Aldrich). The viscosity and surface tension were reported by the manufacturer as 7–12 cP and 33 mN/m at 22 °C, respectively. It has been reported that PEDOT:PSS is a relatively air stable material and its conductivity does not change even after treating for up to 1000 h at 100 °C.⁵³ The bulk conductivity of the ink was measured as 2.6 mS/cm. Jung *et al.* reported on the non-Newtonian behavior of the PEDOT:PSS solution (1.1% polymer + 98.9% water).¹⁸ With increasing shear rate, they observed a power-law relationship in which the viscosity decreases monotonically.

Here, PEDOT:PSS was used to print resistors on flat glass slides and uneven 3D-printed photopolymer-based plastic substrates. The 3D substrates were printed using a desktop 3D ObjetPro printer (StrataSys) to investigate the effect of surface topology on the structure and conductivity of the resistors. Three different topologies were made with different ramp heights (200, 300, and 400 μm) at ramp side angles varying from 40° to 80° by increments of 10°. To be able to print a stable rivulet on a 3D-printed plastic substrate, the receding contact angle needed to be lower than 10°. Therefore, prior to printing, the plastic substrates were treated with air plasma (at 11 W, for 45 s) to achieve the essential receding contact angles. The effect of the surface plasma treatment was investigated using optical contact angle measurements with an OCAH 200 goniometer (DataPhysics Instruments GmbH). The receding and advancing contact angles were $\sim 0^\circ$ and 22° for the flat glass substrates and 8° and 21° for the 3D-printed plastic substrates, respectively.

During the experiments, the room temperature varied between 20 and 25 °C. The humidity was recorded for each experiment and varied between 10% and 60%. We did not observe any variation in droplet generation or the EHD process due to changes in humidity. However, the humidity did influence the evaporation rate of the printed rivulet. Droplet formation was observed using a side-view, high speed camera (Phantom V2011, Vision Research). All images were captured at 180 064 frames-per-second and covered multiple cycles of meniscus pulsation. To facilitate the measurement of resistance, we deposited silver electrodes on top of the printed lines at their edge. The 100 nm conductive silver

electrodes were deposited through a shadow mask to fix their separation distance. The resistance was measured using a standard four-point-probe system (WL210E, Signatone) and a multi-meter (HP3457A).

III. RESULTS AND DISCUSSION

A. Droplet generation in microdripping mode

The emission mode for EHD printing is largely governed by the fluid properties and the applied potential. For PEDOT:PSS, we observed *dripping mode* for weak potential fields, followed by *microdripping mode*, then *unstable cone-jet mode* at higher applied voltages. One cycle of microdripping mode is shown in Figure 2. Early in the cycle, positive charges from the bulk liquid build up at the liquid-air interface due to the applied voltage (Figure 2, phase I). The resulting electric force creates a tangential stress on the liquid surface, thereby elongating the meniscus vertically into a conical shape from which droplets detach. Before the necking starts, the high charge density and high curvature at the meniscus tip causes a high velocity micro-jet of liquid to be expelled (Figure 2, phase II). In order to emit the micro-jet from the apex of the meniscus, the imposed Maxwell stress, given by $\epsilon_0 \epsilon_l V^2 / 2d^2$, where V is the applied voltage, $\epsilon_0 \epsilon_l$ is the liquid permittivity, and d is the stand-off distance, must exceed the local capillary stress; i.e., Rayleigh criterion.^{52,54} The expression for the capillary stress is of the order of γ/R for a spherical cap that acts to restore any interface deformations (γ is the surface tension and R is the radius of curvature of the liquid surface at the cone apex). Emission of the micro-jet results in a drastic reduction in the charge concentration at the meniscus surface. Consequently, the applied electric force decreases significantly and does not pull the meniscus down further. Surface tension forces retract the bulk liquid upwards (Figure 2, phase III), necking begins, and the droplet detachment cycle completes. As long as ink is steadily supplied to the nozzle, this regime will repeat indefinitely and with high periodicity.

In this mode, higher voltages generate smaller droplets at higher frequencies. Microdripping mode is similar to the intermittent single cone-jet mode reported by Juraschek and Röllgen.⁴⁹ This was also reported by Jung *et al.* and is due to charge/mass emission from the apex prior to necking.¹⁸ Moreover, it is noteworthy that microdripping mode is able to generate droplets with diameters an order of magnitude smaller than the nozzle inner diameter. This important feature improves line resolution and limits nozzle fouling.

At voltages below what is required for the onset of microdripping mode, it is possible that a droplet is *not* emitted at every periodic oscillation of the meniscus. At a critical voltage, droplet emission occurs at every oscillation. This critical voltage defines the onset of microdripping mode. The regular emission of a droplet at every pulsation is related to the induced charge accumulation time and is governed by the flow rate, the ink conductivity, and the applied electric field. In microdripping mode, during one oscillation, the potential field is strong enough to induce sufficient charges at the meniscus surface needed for droplet detachment. Moreover, we observed shorter accumulation times at higher voltages, resulting in the generation of smaller droplets.

The surface tension of the working fluid plays a significant role in microdripping mode. Due to the charge concentration on the meniscus interface, the induced repulsive columbic forces between the fluid molecules act against intermolecular attractive forces. This results in a lower *apparent* surface tension for PEDOT:PSS at the meniscus surface.^{55,56} However, this *apparent* surface tension is still not in the range of the required surface tension to establish a stable Taylor cone. Therefore, in microdripping mode, we observed the formation of an evanescent cone-jet at the apex of meniscus. This is due to the lower *apparent* surface tension at the apex compared to the base of meniscus. The local *apparent* surface tension at the apex is not strong enough to retract the mass towards the nozzle, resulting in droplet detachment. The mass ejection reduces the charge concentration at the apex, thereby increasing the local *apparent*

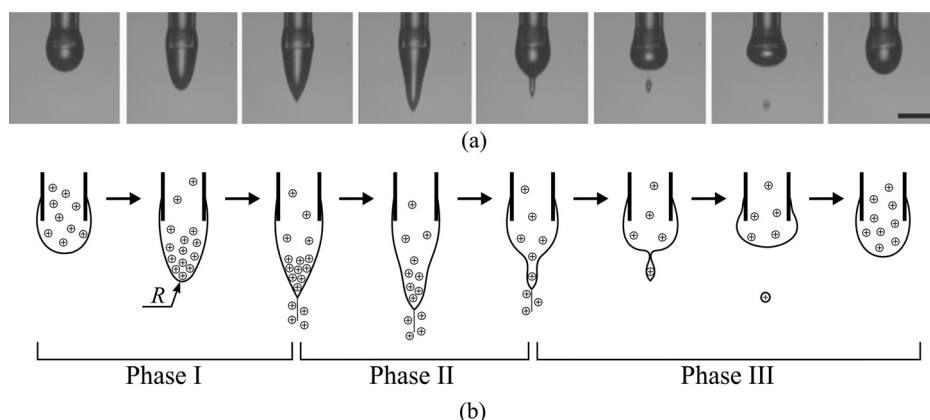


FIG. 2. (a) Micrographs showing different stages of PEDOT:PSS primary droplet detachment in microdripping mode at an applied voltage of 2.8 kV. The time scale between images is 85 μ s. The scale bar denotes 80 μ m. (b) The droplet detachment mechanism is categorized into three major phases. Positive charges in the bulk liquid build up at the interface with the applied voltage. The resulting electric force elongates the meniscus vertically into a conical shape (phase I). Before the necking starts, the high charge density and high curvature at the meniscus tip causes a high velocity micro-jet of liquid to be expelled (phase II). Surface tension forces retract the bulk liquid upwards, necking begins, and the droplet detachment cycle completes (phase III). This process will repeat periodically.

surface tension. The ejection then stops and the meniscus retracts to its original shape and the cycle continues.

Viscosity also plays an important role in microdripping mode since PEDOT:PSS possess a shear-thinning, non-Newtonian behavior. Therefore, it has a high viscosity at low shear rates: 7–12 cP at frequencies less than 10 s^{-1} , which is below the jettable range.¹⁸ However, as shown in Figure 2, the polymer-containing ink shows good microdripping performance. This is because the shear thinning behavior at high shear rates makes the ink jettable, and plays an important factor in microdripping mode.

B. Effect of potential field on droplet generation frequency

We observed that the frequency of droplet generation in microdripping mode is the key parameter that influences the quality of printed features. Figure 3 shows the droplet generation frequency versus applied voltage in microdripping mode for three stand-off distances. The supply flow rate was constant at $0.8 \mu\text{L}/\text{min}$. For larger applied voltages, the droplet generation frequency increases with decreasing separation distance. However, this behavior *reverses* at lower applied voltages; in particular, higher frequencies are achieved at larger stand-off distances. The reason for this relies on the two main contributors to droplet formation in phase I (Figure 2) and their relationship to the Rayleigh limit: (1) the concentration of charges at the meniscus interface and (2) the radius of curvature at the apex of meniscus. Our results (Figure 3) show that at lower voltages, the amount of charge at the interface dictates the droplet generation dynamics; while at higher voltages, the electric field strength drives droplet generation.

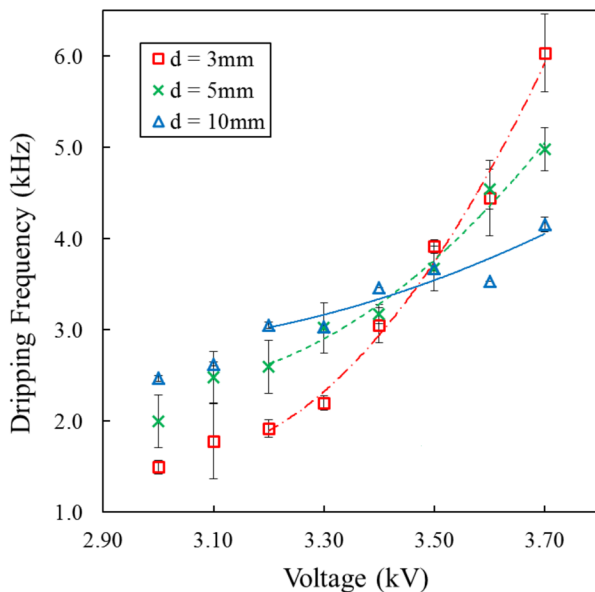


FIG. 3. The effect of applied voltage on droplet generation frequency at three different stand-off distances. The flow rate of PEDOT:PSS was constant at $0.8 \mu\text{L}/\text{min}$. The curves are 2nd order polynomials fitted to the data beyond the critical voltage of 3.10 kV. The R-squared values are larger than 85% in all cases. The error bars are \pm one standard deviation.

To account for this behavior, we use a method of images solution for the electric field induced by the applied potential.⁵⁷ The electric field in the vicinity of the meniscus is

$$E \propto \frac{q_{\text{meniscus}}}{d^2} \propto \frac{V}{d}, \quad (1)$$

where q_{meniscus} is the induced positive charge on the meniscus surface, d is the stand-off distance between the capillary tip and the surface of the target substrate, and V is the applied DC voltage. The amount of accumulated charge is proportional to the stand-off distance and the applied voltage, $q_{\text{meniscus}} \propto Vd$. Therefore, at low voltages, by increasing the distance between the capillary tip and the target substrate, the concentration of induced charge meets the Rayleigh limit more quickly. The droplet generation frequency increases with the applied voltage up to values at which the frequency is greater at shorter stand-off distances. At these high voltages, the meniscus elongation rate due to the applied electric force dominates over the effect of charge concentration at the meniscus apex.

The abrupt increase in the droplet generation frequency with applied voltage is a result of the non-Newtonian, shear thinning behavior of PEDOT:PSS. The decrease in viscosity at high shear rates allows the meniscus to oscillate at the frequencies necessary for microdripping mode.

In Figure 4, the frequency versus applied voltage is shown for ink flow rates of 0.2, 0.8, and $1.2 \mu\text{L}/\text{min}$ in microdripping mode. The range of values for the applied voltage and flow rate were selected to ensure the emission regime was microdripping. All three curves highlight the non-Newtonian behavior of PEDOT:PSS; i.e., the frequency remains constant and then rises significantly at a critical voltage. For a flow rate of $0.2 \mu\text{L}/\text{min}$, there is a smaller range of applied voltages where stable and regular droplet emission

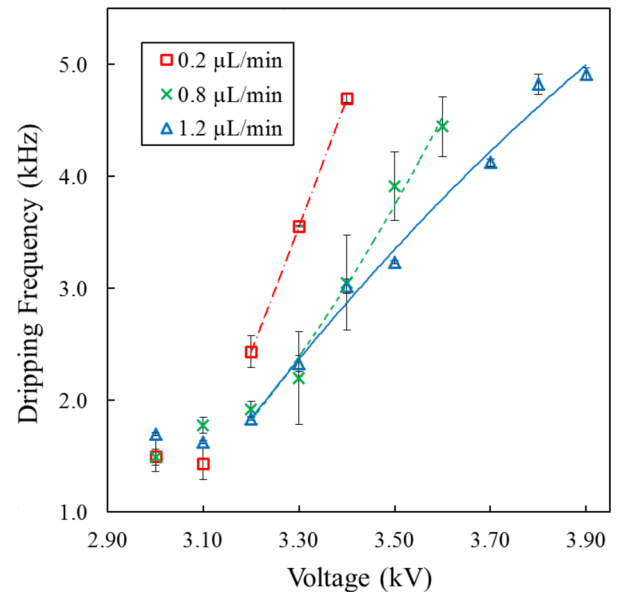


FIG. 4. The effect of applied voltage on droplet detachment frequency for three flow rates. The stand-off distance was constant at 3 mm. The curves are 2nd order polynomials fitted to the data beyond the critical voltage of 3.10 kV. The R-squared values are larger than 98% in all cases. The error bars are \pm one standard deviation.

occurs. This is likely due to the lack of sufficient ink supply at each oscillation, which results in failed or nonuniform droplet emission at higher voltages. Therefore, this defined the minimum possible flow rate for the given nozzle size. At voltages below the critical value, the emission frequency is nearly equal for all three flow rates. This supports our model of droplet detachment in microdripping mode involving the interplay of viscosity, surface tension, and applied potential. None of these parameters depend on the flow rate; therefore, the emission frequency should not vary. However, as a result of mass conservation, larger droplets are expected at greater flow rates.

The last significant parameter that affects the potential field and, consequently, the droplet emission frequency is the susceptibility of the target substrate. The two substrate materials used in this work, glass and Stratus photopolymer, have nearly identical susceptibility. Therefore, the droplet generation frequency versus applied potential and stand-off distance was nearly identical for both materials. Replacing these dielectric substrates with conductive (i.e., metal) substrates did show markedly different behavior. However, for printed electronics applications, conductive substrates cannot be utilized.

C. Alternate printing modes: Dripping and unstable cone-jet

In dripping mode, the growth of the meniscus at the beginning of the cycle takes place in a similar fashion as regular inkjet droplet generation (Figure 5(a)). However, in the presence of the weak potential field, the meniscus does not wet the capillary tube and remains pinned at the tip. This is due to the electrical force directed towards the substrate, which keeps the meniscus contact line balanced against the (upward) capillary force. Necking defines the onset of droplet detachment and governs the droplet size through the force balance between surface tension and primary droplet weight. In the presence of the electric field, the additional applied electric force on the primary droplet balances the surface tension for lower values of droplet weight. Therefore, the emitted droplets possess a smaller size, and detach from the meniscus further from the edge of the emitting nozzle, compared to regular inkjet droplet generation. Consequently, less

accumulation time is needed to form the droplet, and the droplet generation occurs faster (100–500 Hz) than regular droplet detachment (i.e., when no electric potential is applied).

In dripping mode, each primary droplet may be accompanied by the formation of one or more satellite droplets. In Figure 5(a), the main PEDOT:PSS droplet is momentarily connected to the bulk by a linking filament. This filament retracts and creates a secondary droplet. The filament breakage generates capillary waves on the surface of the primary droplet and meniscus. Beside the detachment, the motion of the satellite droplet is of interest. The charge distribution in the bulk liquid and both the primary and satellite droplets exerts a horizontal repulsive force on the satellite droplet. This force causes the small satellite droplets to move off the emission axis at high velocity.

Beyond microdripping mode, the droplet ejection frequency increases with applied voltage. However, at larger voltages and high frequencies, there is not enough time for mass accumulation in each pulsation to occur. Consequently, after each oscillation an excessive charge on the interface cannot be emitted by mass ejection, which results in instabilities in droplet formation (Figure 5(b)). For instance, the detached droplet might impact the vibrating meniscus after detachment and rebound unpredictably, or it may be drawn into the bulk. Therefore, for printing applications, the unstable cone-jet regime should be avoided, because the emitted droplets are not periodic or repeatable.

D. Geometry of printed patterns on flat substrates

Figure 6(a) shows a deposited line printed using microdripping mode on a flat glass substrate. The flow rate and stand-off distance were fixed at $0.8 \mu\text{l}/\text{min}$ and 5 mm, respectively. The droplet generation frequency was sufficiently high to deposit closely spaced micron-size droplets at high printing speeds (up to 50 mm/s). The edges were straight all along the line and no ruptures were observed. The rectangular cross section of the printed line after the solvent is evaporated is illustrated in Figure 6(e). We did not observe significant change in the height of printed lines for different frequencies in microdripping mode. A SEM image of the line (Figure 6(d)) shows that the surface morphology of the

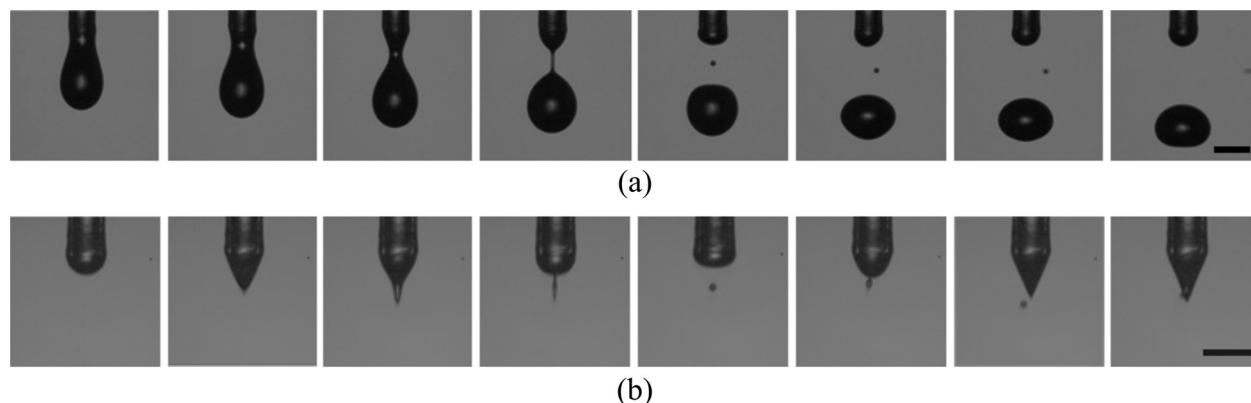


FIG. 5. Different stages of PEDOT:PSS primary droplet detachment in (a) dripping mode at 2.5 kV applied voltage, and (b) unstable cone-jet mode at 3.6 kV applied voltage. The time scale between images at each mode is (a) $95 \mu\text{s}$ and (b) $42 \mu\text{s}$. The scale bars denote $80 \mu\text{m}$.

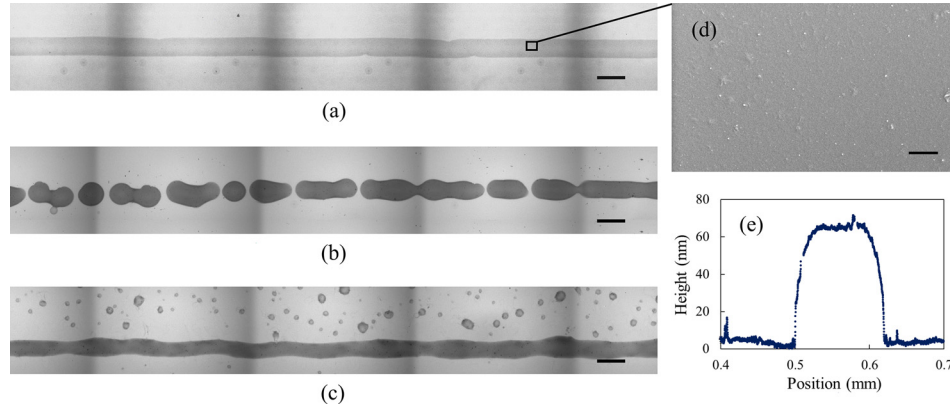


FIG. 6. A line of PEDOT:PSS is printed on flat glass substrate by EHD printing at 5 mm stand-off distance, $0.8 \mu\text{l/min}$ flow rate, and 20 mm/s substrate velocity. For each line the droplets were generated at (a) microdripping mode, 2.8 kV applied voltage, 2.6 kHz frequency, (b) dripping mode, 2.5 kV applied voltage, frequency < 1 kHz, and (c) 3.6 kV applied voltage, 5.3 kHz frequency. The scale bars denote $200 \mu\text{m}$. The images are 5 panels stitched together, (d) SEM image of printed line, the scale bar denotes $3 \mu\text{m}$. (e) The cross section of the printed line in microdripping mode measured by contact profilometry.

printed layer is largely smooth and uniform. Figure 6(b) shows the structure of a deposited line printed using dripping mode at the same flow rate and stand-off distance. The substrate was moved horizontally under the capillary tip at a speed of 20 mm/s. The low droplet generation frequencies achieved in this mode—in the range of 100 to 500 Hz—meant that the stage speed (20 mm/s) was too high to form a continuous line. Therefore, this mode does not provide reliably continuous lines at the desired high translation speeds despite the fact that the deposited droplet diameters were about 3–4 times greater than the capillary tip inner diameter.

Figure 6(c) shows the structure of a deposited line printed using the unstable cone-jet mode. The flow rate, stand-off distance, and substrate velocity were $0.8 \mu\text{l/min}$, 5 mm, and 20 mm/s, respectively. Many of the generated droplets were emitted erratically, and did not detach vertically downwards in this mode. Therefore, many of the emitted droplets landed over a wide area. While the frequency was high enough to create a continuous line, it often would possess ruptures caused by the instabilities in droplet generation.

These results show that microdripping mode is the preferred regime for EHD printing of functional inks like PEDOT:PSS. This mode provides small and uniform droplets, excellent repeatability and line quality, large stand-off distances, and high print speeds. It is clear that dripping mode and unstable cone-jet mode are not suitable operating regimes for materials printing.

E. Resistance of lines printed using microdripping mode

To demonstrate the capability of EHD printing in microdripping mode, we printed resistive elements on flat and uneven substrates. Resistors were selected given their ubiquity in electronic devices. Only the microdripping mode was considered given its superior properties over the other operating regimes. The average resistance per resistor length and line width was measured for varying substrate velocities. The stand-off distance and applied voltage were maintained constant at 3 mm and 3.3 kV, respectively, for three ink supply flow rates of 0.2, 0.8, and $1.2 \mu\text{l/min}$.

The substrate velocity is expressed in non-dimensional form as

$$\pi_1 = \frac{U_{sub}}{(f_{gen}^2 Q)^{1/3}}, \quad (2)$$

where U_{sub} is the substrate velocity, f_{gen} is the droplet generation frequency, and Q is the ink flow rate.

Since the Bond number for a landed droplet after impinging is on the order of 10^{-4} , we use a spherical cap approximation to solve for the radius of an individual sessile droplet R_0 deposited on the substrate. We consider R_0 as the characteristic length scale, which can be expressed as

$$R_0 = \sqrt[3]{\frac{3}{\pi(2 - 3 \cos \theta + \cos^3 \theta)}} (V_{drop})^{1/3}, \quad (3)$$

where $V_{drop} = Q/f_{gen}$ and θ is taken as the advancing contact angle ($\theta_{adv} = 22^\circ$ for the glass substrate).

The width of a printed line is expressed in non-dimensional form as

$$\pi_2 = \frac{W}{R_0}, \quad (4)$$

where W is the line width. In Figure 7, the non-dimensional line width (π_2) is plotted as a function of the non-dimensional substrate velocity (π_1). A power law relationship exists between the substrate velocity and the line width; i.e., $\pi_2 = C\pi_1^{-0.5}$, where C is a constant that depends on the properties of the ink and substrate. Dimensionally, the range of line widths achieved in this study was between 50 and $500 \mu\text{m}$.

The quantity U_{sub}/f_{gen} represents the spacing between consecutive droplets deposited on the substrate. As its value decreases, the width of the printed line grows rapidly. For slow substrate velocities (U_{sub}), the generated droplets land closely spaced on the substrate and expand the edge of the rivulet, resulting in a large resistor width. Conversely, the minimum theoretical line width of a printed resistor is $W_{min} = 2R_0$, which would occur when U_{sub} is at its maximum and there is point contact between adjacent droplets. Note that in Figure 7,

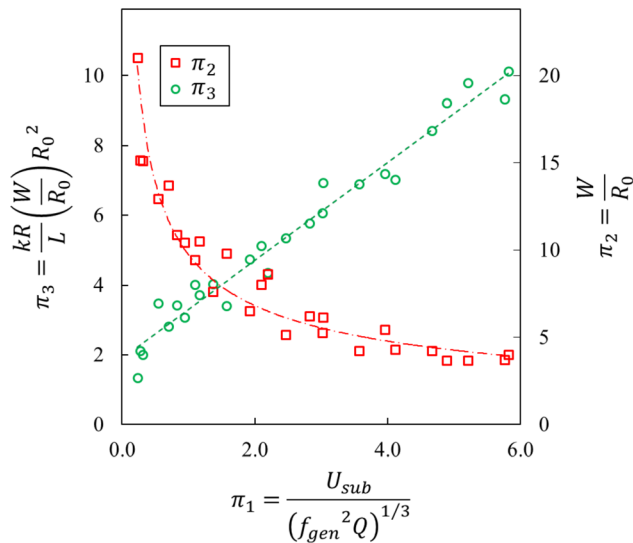


FIG. 7. The red power curve fitted on the square data set indicates the relation between the characteristic resistor width (π_2) and the characteristic droplet spacing (π_1). The green dashed line is fitted on the circle data set, representing a linear relation between dimensionless resistance per length (π_3) versus the characteristic droplet spacing (π_1). The stand-off distance and applied voltage were maintained constant at 3 mm and 3.3 kV, respectively, for three ink supply flow rates 0.2, 0.8, and 1.2 $\mu\text{l}/\text{min}$. The R-squared value for the fitted solid power curve and the dashed line are 93% and 97%, respectively.

for increasing values of π_1 , π_2 approaches a value of 2. In practice, adjacent droplets must be overlapping to create a robust continuous line; therefore, the printed line widths are notably wider than the theoretical limit.

The resistance per unit length of the printed resistor is expressed in non-dimensional form as

$$\pi_3 = \frac{kR}{L} \left(\frac{W}{R_0} \right) R_0^2, \quad (5)$$

where R/L is the resistance per length and k is the PEDOT:PSS dry film conductivity. For all printing conditions, k was 150 S/m, which is similar to values reported in the literature.^{58,59} In Figure 7, the non-dimensional resistance (π_3) is plotted as a function of the non-dimensional substrate velocity (π_1). A linear relationship exists between the substrate velocity and line resistance; i.e., $\pi_3 = F\pi_1$, where F is a constant that depends on the properties of the ink and substrate. Dimensionally, the range of resistance values achieved was between 1 and 70 $\Omega/\mu\text{m}$.

F. Characterization of printed patterns on uneven substrates

The photopolymer used by the StrataSys Objet 3D Printer was Transparent VeroClear—a nearly colorless

material with properties similar to transparent thermoplastics like poly(methyl methacrylate) (PMMA). This material was used to fabricate uneven substrates as the target surface to print transparent PEDOT:PSS resistors. To investigate the effects of substrate topology, we 3D printed a model geometric feature of a step with ramped sides (Figure 8(a)). The operating conditions for EHD printing were fixed at 3 mm stand-off distance, 0.8 $\mu\text{l}/\text{min}$ flow rate, 5 mm/s substrate velocity, and 4.2 kV applied voltage.

Figure 8(a) shows a representative substrate with five symmetrical ramps. The ramps have varying heights and sloping angles at the leading and trailing edges. We selected the ramp shapes as basic model geometries to investigate the effects of substrate topology on EHD print performance. The use of basic models was useful to gain fundamental insight into the effect of topology on the process-structure-property relationship of EHD printing.

We defined two parameters to investigate the effect of uneven topology on the line structure: (1) wetting angle, which is the interior angles on both edges of the line at the corner of the ramp on the lower surface (Figure 8(b)), and (2) neck shrinkage ratio, which is the ratio of the necking width to the wetted width at the corner of the ramp (Figure 8(b)). Figure 9 shows the structure of a PEDOT:PSS line printed across the ramp-shaped topology with differing heights. To measure the wetting angle, a line was drawn tangent to the edge of the deposit that intersected with the projection of the slope (indicated by the dark region in Figures 8(b) and 9). The interior angle was then calculated using ImageJ. The necking width was defined as the minimum width of the printed line at the bottom of the ramp. An enhanced image of the line printed along the slope is shown in Figure 9(d).

The wetting angle decreases linearly with the leading/trailing ramp side angle for three different step heights (Figure 10). This trend is likely due to the surface wettability inside a corner. The deposited rivulet on the lower surface beside the ramp is placed in a tighter corner for a steeper leading/trailing side angle. This geometry creates a multi-curvature surface on the rivulet, which drives wetting along the ramp. Consequently, a larger wetting width and shorter necking width is expected due to the higher curvature for steeper leading/trailing side angles (Figure 11). In Figure 11, a linear decrease in the neck shrinkage ratio is observed with increasing ramp side angle. This confirms more wetting at the corner of steeper ramps, as well as smaller wetting angles.

Moreover, as seen in Figure 10, at a fixed leading/trailing side angle, wider wetted regions are observed for larger

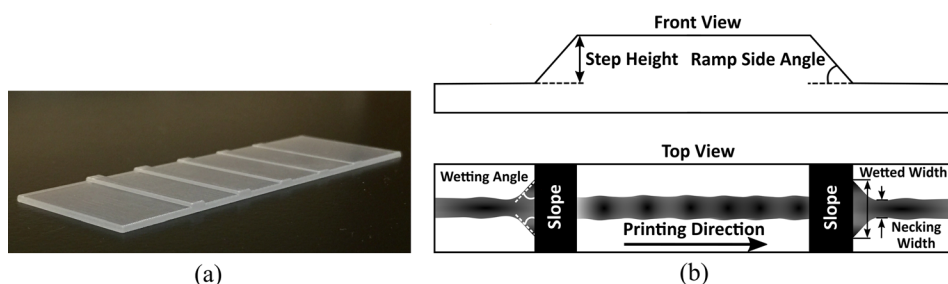


FIG. 8. (a) Photopolymer-based 3D-printed substrate consisting of five ramps. This substrate is used to study the effects of substrate topology on the performance of EHD printing. (b) The wetting angle and the neck shrinkage ratio describing the structure of the deposited line over the leading and trailing edges.

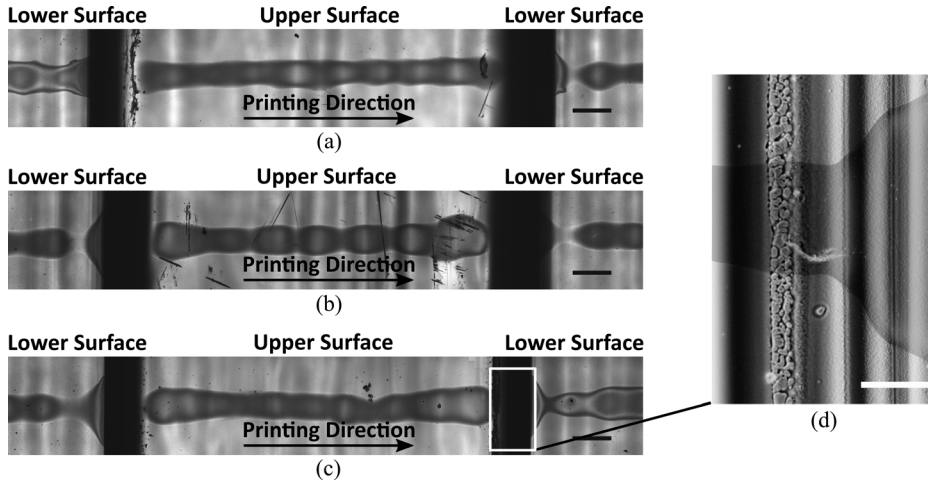


FIG. 9. Different structures of printed PEDOT:PSS lines across a ramp-shape topology at 40° leading and trailing edges: (a) $200\ \mu\text{m}$ high, (b) $300\ \mu\text{m}$ high, (c) $400\ \mu\text{m}$ high, the scale bars denote $300\ \mu\text{m}$. (d) Micrograph of the line printed along the slope of the ramp. The contrast of the deposit is enhanced for clarity since the slope made it difficult to capture a clear image. The scale bar denotes $100\ \mu\text{m}$.

step heights. This is likely due to the longer length of the leading/trailing sides of the ramp for larger steps. These longer slopes acquire more deposited fluid on them, which can migrate toward the lower surface (under gravity) and cause longer wetting widths. The smaller values for both wetting angles and neck shrinkage ratios for higher ramp step heights seen in Figures 10 and 11 support this observation (arrows).

The resistance versus ramp side angle of a resistor printed across the leading/trailing side of a ramp for two step heights is shown in Figure 12. For both heights, the resistance increases linearly with the ramp leading/trailing side angle and the resistance was lower for the taller ramp. This may be due to the displacement of the deposited fluid from the leading/trailing sides toward the lower surfaces (due to gravity). This neutralized the effects of the neck shrinkage, ultimately decreasing the resistance. Note that repeatable continuous lines could not be achieved at the maximum ramp step height of $400\ \mu\text{m}$, so the resistance for this case was not plotted.

IV. SUMMARY

In this work, a tunable electrohydrodynamic (EHD) printing method capable of generating micron-sized droplets with controllable size was presented. The main advantages of EHD printing operating in microdripping mode are high printing speeds, large stand-off distances, droplet diameters an order of magnitude smaller than the nozzle opening, and minimal instrumentation requirements. In addition, further reductions in the nozzle dimensions may enable even finer resolution approaching the sub-micron scale.

An array of emission modes for EHD printing was reported. Depending on the strength of the applied potential field, three modes were observed for PEDOT:PSS. Microdripping mode was created in the presence of a moderate potential field. This mode generated droplets 10 times smaller than the nozzle inner diameter at frequencies in excess of 5 kHz. The effect of flow rates, applied voltage, and stand-off distance on droplet generation frequency was reported. We observed that the frequency increased

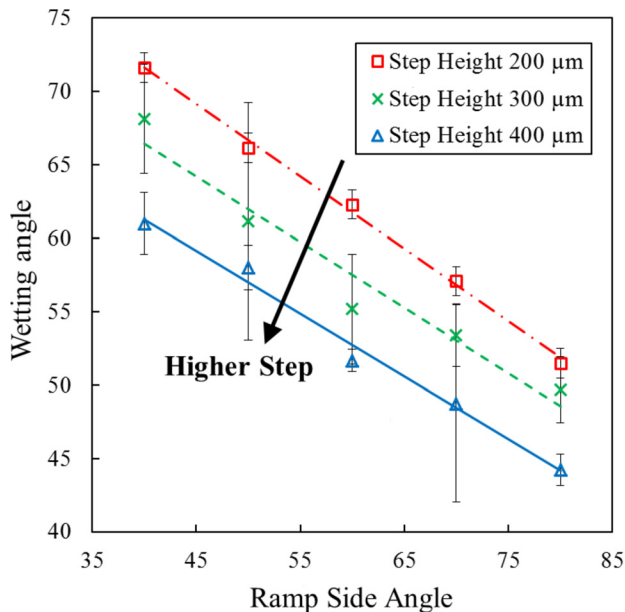


FIG. 10. Wetting angle versus ramp leading/trailing side angle. Each line is plotted at a different ramp height. The error bars are \pm one standard deviation.

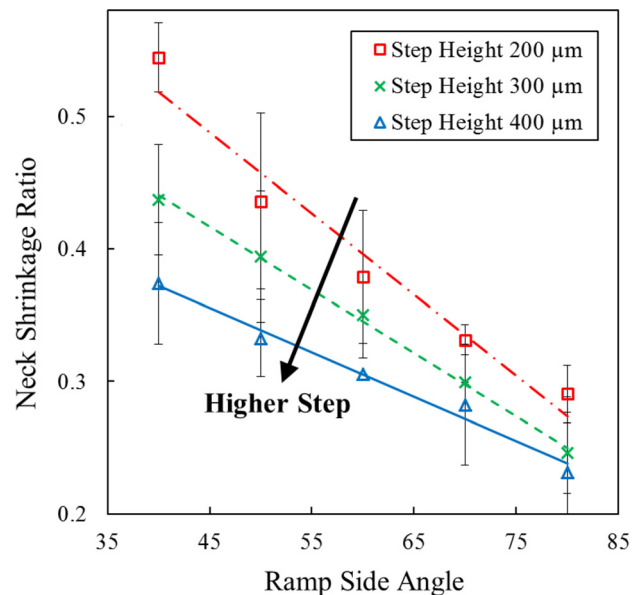


FIG. 11. Neck shrinkage ratio versus ramp leading/trailing side angle. Each line is plotted at a different ramp height. The error bars are \pm one standard deviation.

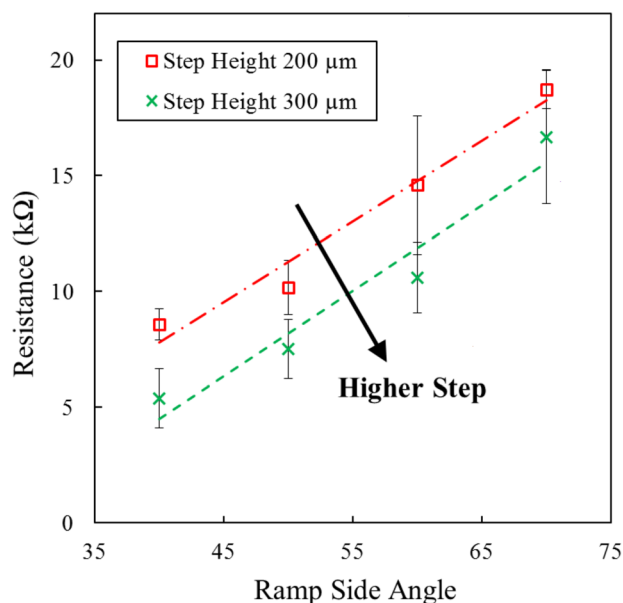


FIG. 12. Resistance versus ramp leading/trailing side angle. Each line is plotted at a different ramp height. The resistance is measured between the bottom and top of the ramp. The error bars are \pm one standard deviation.

nonlinearly with the applied voltage, which is strongly influenced by the non-Newtonian shear thinning effect of PEDOT:PSS and the supply flow rate. The microdripping mode was used to print resistors on flat glass substrates. Data were presented that can be used to select the optimum substrate velocity and flow rate to print an organic resistor with the desired resistance.

The topology of a 3-dimensional target substrate was shown to have a significant effect on the structure and function of a printed resistor. We defined two parameters to characterize the structure of a printed line near a model geometric feature (a 3D printed ramp): wetting angle and neck shrinkage ratio. For steeper ramps, the printed rivulet wets more along the ramp edge. The resistance was measured at the leading/trailing sides of the ramp and included the necking regions. It was found that the resistance increased linearly with increasing ramp side angle.

¹V. Subramanian, J. M. Fréchet, P. C. Chang, D. C. Huang, J. B. Lee, S. E. Moles, A. R. Murphy, D. R. Redinger, and S. K. Volkman, *Proc. IEEE* **93**, 1330 (2005).

²C. N. Hoth, P. Schilinsky, S. A. Choulis, and C. J. Brabec, *Nano Lett.* **8**, 2806 (2008).

³J. Dijkman, P. Duineveld, M. Hack, A. Pierik, J. Rensen, J.-E. Rubingh, I. Schram, and M. Vernhout, *J. Mater. Chem.* **17**, 511 (2007).

⁴M. Caironi, E. Gili, T. Sakanoue, X. Cheng, and H. Sirringhaus, *ACS Nano* **4**, 1451 (2010).

⁵H. Minemawari, T. Yamada, H. Matsui, J. y. Tsutsumi, S. Haas, R. Chiba, R. Kumai, and T. Hasegawa, *Nature* **475**, 364 (2011).

⁶D. Bailo, A. Generosi, V. R. Albertini, R. Caminiti, R. De Bettignies, and B. Paci, *Synth. Met.* **162**, 808 (2012).

⁷P. Wilson, C. Lekakou, and J. F. Watts, *Org. Electron.* **13**, 409 (2012).

⁸B. Friedel, T. J. Brenner, C. R. McNeill, U. Steiner, and N. C. Greenham, *Org. Electron.* **12**, 1736 (2011).

⁹Z. A. King, C. M. Shaw, S. A. Spanninga, and D. C. Martin, *Polymer* **52**, 1302 (2011).

¹⁰S. A. Mauger, L. Chang, C. W. Rochester, and A. J. Moulé, *Org. Electron.* **13**, 2747 (2012).

¹¹A. Elschner, S. Kirchmeyer, W. Lovenich, U. Merker, and K. Reuter, *PEDOT: Principles and Applications of an Intrinsically Conductive Polymer* (CRC Press, 2010).

¹²S. Kirchmeyer and K. Reuter, *J. Mater. Chem.* **15**, 2077 (2005).

¹³J. A. Lim, J. H. Cho, Y. D. Park, D. H. Kim, M. Hwang, and K. Cho, *Appl. Phys. Lett.* **88**, 082102 (2006).

¹⁴R. Mannerbro, M. Rånklöf, N. Robinson, and R. Forchheimer, *Synth. Met.* **158**, 556 (2008).

¹⁵T. Aernouts, P. Vanlaeke, W. Geens, J. Poortmans, P. Heremans, S. Borghs, R. Mertens, R. Andriessen, and L. Leenders, *Thin Solid Films* **451**, 22 (2004).

¹⁶J. Y. Kim, K. Lee, N. E. Coates, D. Moses, T.-Q. Nguyen, M. Dante, and A. J. Heeger, *Science* **317**, 222 (2007).

¹⁷J. Tarver and Y. Loo, *Handbook of Nanoscale Optics and Electronics* (Elsevier, 2010), p. 107.

¹⁸S. Jung, A. Sou, E. Gili, and H. Sirringhaus, *Org. Electron.* **14**, 699 (2013).

¹⁹A. Chiolerio, P. Rivolo, S. Porro, S. Stassi, S. Ricciardi, P. Mandracci, G. Canavese, K. Bejtka, and C. F. Pirri, *RSC Adv.* **4**, 51477 (2014).

²⁰S.-I. Na, B.-K. Yu, S.-S. Kim, D. Vak, T.-S. Kim, J.-S. Yeo, and D.-Y. Kim, *Sol. Energy Mater. Sol. Cells* **94**, 1333 (2010).

²¹Y. H. Kim, C. Sachse, M. L. Machala, C. May, L. Müller-Meskamp, and K. Leo, *Adv. Funct. Mater.* **21**, 1076 (2011).

²²J. Kim, J. Jung, D. Lee, and J. Joo, *Synth. Met.* **126**, 311 (2002).

²³J. Ouyang, C. W. Chu, F. C. Chen, Q. Xu, and Y. Yang, *Adv. Funct. Mater.* **15**, 203 (2005).

²⁴S. Jönsson, J. Birgersson, X. Crispin, G. Greczynski, W. Osikowicz, A. D. Van Der Gon, W. R. Salaneck, and M. Fahlman, *Synth. Met.* **139**, 1 (2003).

²⁵A. M. Nardes, R. A. Janssen, and M. Kemerink, *Adv. Funct. Mater.* **18**, 865 (2008).

²⁶Y. Kim, J. Lee, H. Kang, G. Kim, N. Kim, and K. Lee, *Sol. Energy Mater. Sol. Cells* **98**, 39 (2012).

²⁷E. Tekin, P. J. Smith, and U. S. Schubert, *Soft Matter* **4**, 703 (2008).

²⁸B. Derby, *Annu. Rev. Mater. Res.* **40**, 395 (2010).

²⁹S. Jung and I. M. Hutchings, *Soft Matter* **8**, 2686 (2012).

³⁰Y. Liu, T. Cui, and K. Varshneyan, *Solid-State Electron.* **47**, 1543 (2003).

³¹B. Chen, T. Cui, Y. Liu, and K. Varshneyan, *Solid-State Electron.* **47**, 841 (2003).

³²T. Kawase, H. Sirringhaus, R. H. Friend, and T. Shimoda, *Adv. Mater.* **13**, 1601 (2001).

³³Z. Xiong and C. Liu, *Org. Electron.* **13**, 1532 (2012).

³⁴I. Clancy, G. Amarandei, C. Nash, and B. Glowacki, *J. Appl. Phys.* **119**, 054903 (2016).

³⁵S. Jeong, H. C. Song, W. W. Lee, Y. Choi, and B.-H. Ryu, *J. Appl. Phys.* **108**, 102805 (2010).

³⁶J. Choi, Y.-J. Kim, S. Lee, S. U. Son, H. S. Ko, V. D. Nguyen, and D. Byun, *Appl. Phys. Lett.* **93**, 193508 (2008).

³⁷V. D. Nguyen and D. Byun, *Appl. Phys. Lett.* **94**, 173509 (2009).

³⁸J. B. Szczech, C. M. Megaridis, D. R. Gamota, and J. Zhang, *IEEE Trans. Electron. Packag. Manuf.* **25**, 26 (2002).

³⁹J. S. Kim, W. S. Chung, K. Kim, D. Y. Kim, K. J. Paeng, S. M. Jo, and S. Y. Jang, *Adv. Funct. Mater.* **20**, 3538 (2010).

⁴⁰M. Cloupeau and B. Prunet-Foch, *J. Aerosol Sci.* **25**, 1021 (1994).

⁴¹I. Hayati, A. Bailey, and T. F. Tadros, *J. Colloid Interface Sci.* **117**, 205 (1987).

⁴²J. Zeleny, *Phys. Rev.* **10**, 1 (1917).

⁴³J. Zeleny, "On the condition of instability of electrified drops, etc," *Proc. Camb. Phil. Soc.* **18**, 71 (1915).

⁴⁴J. Fernández de La Mora, *Annu. Rev. Fluid Mech.* **39**, 217 (2007).

⁴⁵H. Kim, J. Song, J. Chung, and D. Hong, *J. Appl. Phys.* **108**, 102804 (2010).

⁴⁶K. Sung and C. S. Lee, *J. Appl. Phys.* **96**, 3956 (2004).

⁴⁷G. Taylor, *Disintegration of Water Drops in an Electric Field* (The Royal Society, 1964), p. 383.

⁴⁸M. Mutoh, S. Kaieda, and K. Kamimura, *J. Appl. Phys.* **50**, 3174 (1979).

⁴⁹R. Juraschek and F. Röhlgen, *Int. J. Mass Spectrom.* **177**, 1 (1998).

⁵⁰J.-U. Park, M. Hardy, S. J. Kang, K. Barton, K. Adair, D. Kishore Mukhopadhyay, C. Y. Lee, M. S. Strano, A. G. Alleyne, and J. G. Georgiadis, *Nat. Mater.* **6**, 782 (2007).

⁵¹C.-H. Chen, D. Saville, and I. Aksay, *Appl. Phys. Lett.* **89**, 124103 (2006).

⁵²H.-C. Chang and L. Y. Yeo, *Electrokinetically Driven Microfluidics and Nanofluidics* (Cambridge University Press, Cambridge, UK, 2010).

- ⁵³J. Huang, P. F. Miller, J. S. Wilson, A. J. de Mello, J. C. de Mello, and D. D. Bradley, *Adv. Funct. Mater.* **15**, 290 (2005).
- ⁵⁴L. Rayleigh, London, Edinburgh, *Dublin Philos. Mag. J. Sci.* **14**, 184 (1882).
- ⁵⁵E. Davis and M. Bridges, *J. Aerosol Sci.* **25**, 1179 (1994).
- ⁵⁶B. Vonnegut and R. L. Neubauer, *J. Colloid Sci.* **7**, 616 (1952).
- ⁵⁷D. J. Griffiths and R. College, *Introduction to Electrodynamics* (Prentice Hall, Upper Saddle River, NJ, 1999), Vol. 3.
- ⁵⁸T. Stöcker, A. Köhler, and R. Moos, *J. Polym. Sci., Part B: Polym. Phys.* **50**, 976 (2012).
- ⁵⁹K.-C. Chang, M.-S. Jeng, C.-C. Yang, Y.-W. Chou, S.-K. Wu, M. A. Thomas, and Y.-C. Peng, *J. Electron. Mater.* **38**, 1182 (2009).